Journal of Applied Physics

RESEARCH ARTICLE | APRIL 15 2026

Pressure amplification in single-stage gas launchers via Mach-stem formation

B. Dias ; R. L. Doherty ; J. Shadbolt ; V. Beltrán ; E. Escauriza ; D. J. Chapman ;
D. E. Eakins ; A. Rack ; H. W. Doyle ; M. G. Gorman

J. Appl. Phys. 139, 155901 (2026)
https://doi.org/10.1063/5.0323238

AIP Publishing

Journal of
Applied Physics

METHOD

pubs.aip.org/aip/jap

Pressure amplification in single-stage gas launchers via Mach-stem formation

Cite as: J. Appl. Phys. **139**, 155901 (2026); doi: 10.1063/5.0323238
Submitted: 16 January 2026 · Accepted: 29 March 2026 ·
Published Online: 15 April 2026

View Online Export Citation CrossMark

B. Dias,[1,a)] R. L. Doherty,[1] J. Shadbolt,[1] V. Beltrán,[1] E. Escauriza,[2] D. J. Chapman,[3] D. E. Eakins,[3] A. Rack,[4] H. W. Doyle,[1] and M. G. Gorman[1]

AFFILIATIONS

[1] First Light Fusion Ltd., Unit 9 and 10 Oxford Pioneer Park, Yarnton, Oxford OX5 1QU, Oxfordshire, United Kingdom
[2] Department of Physics, University of California San Diego, La Jolla, California 92093, USA
[3] Department of Engineering Science, University of Oxford, Oxford OX1 3PJ, United Kingdom
[4] ESRF—The European Synchrotron, 38043 Grenoble, France

[a)] **Author to whom correspondence should be addressed:** bruce.dias@firstlightfusion.com. **URL:** www.firstlightfusion.com

ABSTRACT

We present a pressure amplifier that integrates with single-stage gas launchers and enhances the accessible range of sample pressure states. The design of the amplifier was guided by hydrodynamic simulations. Using a convergent shock geometry, the amplifier generates pressures of up to 4.3 times greater than those achievable through direct impact. The evolution of the shock fronts through the amplifier was captured using ultrahigh speed x-ray phase-contrast imaging, and the velocity history of shocked samples was measured using photonic Doppler velocimetry to ascertain output pressures of the amplifier. Pressures of up to 40 GPa were observed in copper and iron samples as well as the observation of phase-transition kinetics in iron (α–ϵ transition). These results demonstrate the utility of the pressure amplifier in allowing a wider range of material phase space to be explored with single-stage guns.

I. INTRODUCTION

Single-stage gas launchers or gas guns (SSGGs) are widely used in scientific research due to their simplicity, reliability, and cost-effectiveness. Their use plays a key role in impact physics, planetary science, high-pressure equation-of-state (EOS) studies, and the study of material dynamics.[1–5] However, the velocities and resulting impact pressures achievable with single-stage gas launchers are limited by physical and engineering constraints. These include the maximum reservoir pressure and, most critically, the restricted gas flow rate through diaphragms that separate the reservoir from the launch tube.[2,6] Single-stage gas launchers can operate with velocities exceeding 1.6 km/s in well-optimized systems.[7] However, more typical single-stage gas launchers are limited to velocities of $\leq$0.8 km/s. Such velocities translate to relatively low impact pressures: for example, 0.8 km/s aluminum flyers generate approximately 2.5 GPa in polymers, while impacts on higher-impedance materials, such as copper or iron, can produce pressures up to 10 GPa.

To achieve higher velocities and impact pressures, two-stage[8,9] and three-stage gas gun[10] systems have been employed. These drivers provide significantly improved velocities[11] greater than 9 km/s, with some systems[12] reaching velocities exceeding 11 km/s equating to impact pressures greater than 380 and 570 GPa in polymers and metals, respectively. However, multi-stage systems involve higher upfront costs, greater system complexity, and increased operational and infrastructure demands. This paper presents a pressure amplifier that uses convergent shocks and Mach stem interactions to greatly enhance the shock pressure imparted on a sample of interest by a single-stage gas launcher. The amplifiers were demonstrated on two 25 mm bore single-stage gas launcher systems, similar to that previously reported by Rack *et al.*[13] Pressure amplification through converging shocks has been demonstrated using several distinct approaches. Polymer pusher–impactor assemblies generate inertial geometric focusing in metallic cones.[14] Explosively driven conical waveguides similarly strengthen shocks through guided convergence and internal Mach-stem formation.[15] Shock-tube systems with smoothly converging sections transform planar shocks into stronger spherical or cylindrical waves, extending achievable pressures.[16] Laser-driven annular targets have also produced centrally converging shocks and controlled Mach-stem formation in gas environments.[17] These methods illustrate the range of hydrodynamic amplification strategies but differ markedly from the compact modular single-stage gas-gun driven Mach-stem amplifier used in the present work, designed as a simple addition to muzzle of a single-stage launcher. A key objective of this work was not only to measure the amplified output pressure, but also to directly study the internal shock dynamics that give rise to the amplification. At the European Synchrotron Radiation Facility (ESRF), ultrahigh speed x-ray imaging (UHS XRI)[13,18,19] enabled time-resolved visualization of shock-front dynamics within the amplifier. These measurements provided the opportunity to validate the behavior predicted by hydrodynamic simulations, including the timing and geometry of shock convergence and recombination features that are essential to the design and optimization of pressure amplifiers. Additional experiments at the University of Oxford used photonic Doppler velocimetry (PDV)[20] to characterize the velocity history and peak pressures delivered to various samples.

Experimental observations indicate sample pressure enhancements of up to 4.3 times vs the direct impact (defined in Sec. III C) of an Al projectile. In shocked iron, multiple waves consistent with the $\alpha \rightarrow \varepsilon$ transformation were observed, with peak sample pressures reaching 40 GPa. Together, these results demonstrate that pressure amplifiers enable SSGGs with modest projectile velocities to access significantly larger regions of material phase space.

II. SINGLE-STAGE GAS LAUNCHER PRESSURE AMPLIFIER

A. Amplifier mechanisms

The pressure amplifier is designed as a simple add-on to existing SSGG systems, intended to be mounted directly to the end of the launch-tube and impacted by a metallic tipped projectile. Samples of interest can be bonded directly to the amplifier exit to enable studies at elevated pressures. The pressure amplifier is made up of a conical cavity, filled with a low impedance UV cure resin, encased by a thick high impedance wall (anvil) made of steel. The conical cavity is characterized by a convergence ratio (CR) defined by its input and output diameters of 20 and 3 mm ($\text{CR} = 6.6$), respectively. The input diameter is intentionally undersized relative to the projectile tip to accommodate typical impact concentricity tolerances of single-stage gas launchers (≤ 10 mrad tilt).[21] This geometric margin ensures reliable full engagement under expected alignment variations. A dedicated sensitivity study examining small lateral offsets or impact tilt was not performed in the present work, as the current design operates within established alignment tolerances for planar-impact experiments. A detailed investigation aimed at minimizing concentricity and tilt sensitivity would require full 3D simulations and is considered beyond the scope of this study, although it forms part of future design refinement. Previous work using amplifiers of similar geometry[22] has shown that impact tilts exceeding 1° primarily introduce degradation in output-shock planarity. Since this aspect was not optimized in the present design, the impact tilt of projectiles used here was not of immediate concern. Two amplifier designs with differing cone angles (and lengths) are presented here, with similar operating mechanisms.

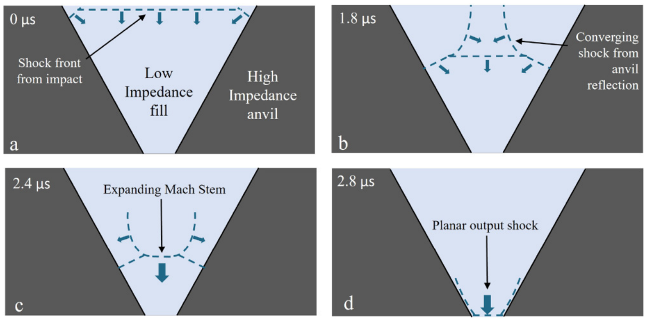

FIG. 1. Evolution of a projectile-driven planar input shock wave through a conical pressure amplifier, with a single on-axis Mach stem crossing. (a) Projectile impact generates a planar shock. (b) Shock reflections from the anvil generate converging Mach reflections, while the main shock continues propagating. (c) The Mach reflections coalesce and cross on-axis to form an expanding Mach stem. (d) The Mach stem expands, forming a planar shock at the output.

Figure 1 illustrates the working principle of a basic conical pressure amplifier. The projectile impacts the amplifier, launching a planar shock wave through the low impedance resin fill. Simultaneously, Mach reflections[23,24] occur at the high impedance steel anvil [Fig. 1(a)]. These Mach reflections propagate toward the central axis as the planar shock front continues to advance through the amplifier [Fig. 1(b)]. All three shock fronts coalesce on-axis to form a Mach stem[25,26] that expands as a new planar shock front [Fig. 1(c)]. The planar Mach stem, which is considerably stronger than the input shock generated by the projectile impact, grows to fill the output area of the amplifier [Fig. 1(d)]. The working principle of a second longer amplifier (with a smaller cone angle) is outlined in Fig. 2. The projectile impact again launches a planar shock front through the amplifier with converging Mach reflections [Figs. 2(a) and 2(b)]. The shock fronts coalesce on-axis to form a Mach stem [Fig. 2(c)]. However, the longer cone means that reflections from the anvil walls occur again, causing a second pair of inward moving Mach reflections [Fig. 2(d)]. These oblique shock fronts coalesce on-axis for a second time to form a new Mach stem, which expands to fill the output of the amplifier [Figs. 2(e) and 2(f)]. Again, the Mach stem is considerably higher pressure than the initial impact pressure.

B. Amplifier design and simulations

The design of pressure amplifiers requires careful hydrodynamic modeling to precisely time the convergence of multiple shock fronts. Simulations were carried out using our internal hydrodynamics code B2,[27] which contains pre-computed EoS tables created using the Frankfurt EOS (FEOS) code,[28] as well as closure microphysics tables.[29]

A cone angle scan was performed while keeping the CR and material set fixed. Iron was considered for the anvil material, while poly(methyl methacrylate) (PMMA) was used to represent the UV-cured resin fill material. These are not the exact materials used

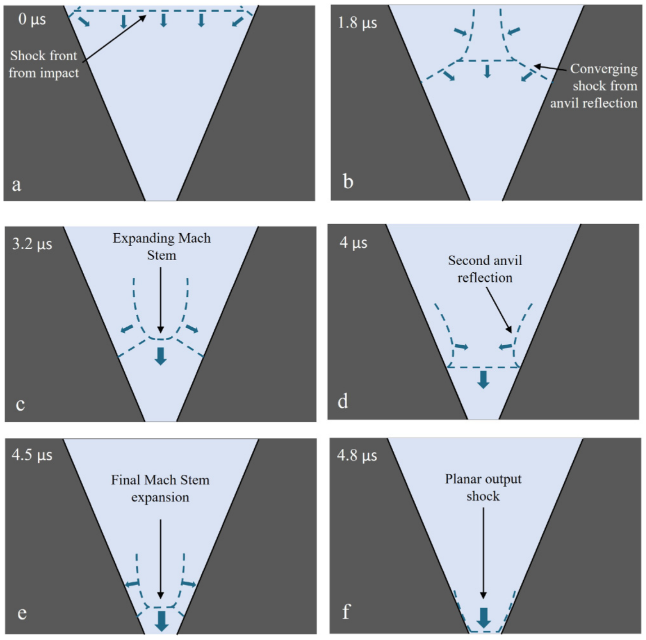

FIG. 2. Evolution of the shock wave through a longer conical pressure amplifier, with two on-axis Mach stem crossings. Panels (a)–(c) show the same sequence as Figs. 1(a)–1(c). Following on-axis crossing, the expanding fronts reflect off the anvil and again converge inward. (e) The process repeats, with the reflected converging fronts crossing on-axis, forming a second expanding Mach stem. (f) The Mach-stem continues to expand and unloads at the output.

TABLE I. Geometry and material parameters for standard and thin-walled amplifier designs.

Parameter	Standard	Thin-wall
Geometric parameters		
Cone angle (°)	75/45	75/45
Cone length (mm)	11.1/20.5	11.1/20.5
Input diameter (mm)	20.0	20.0
Output diameter (mm)	3.0	3.0
Wall thickness at inlet (mm)	10.0	10.0
Wall thickness at outlet (mm)	18.5	2.0
Thin-out distance (mm)	N/A	5.1/10.5
Materials		
Anvil-wall material	Steel 316L	Al 6082
Fill resin	Dymax 6-621	
Fill density (g $\mathrm{cm^{-3}}$)	1.08	

in manufacturing (see Table I), but were adopted at this stage because equation-of-state (EoS) models were available and their impedances are comparable to those of the manufacturing materials. Cone angles of 45° and 75° were selected, as these configurations produced correctly timed Mach stem formation and subsequent expansion at the amplifier output (Figs. 1 and 2). Further optimization of the design with alternative geometries, convergence ratios, or material combinations was not explored in this study.

To enable phase-contrast imaging (PCI) of the shock dynamics within the amplifier, a modified aluminum thin-walled design was developed for experiments conducted at the ESRF. The aim was to reduce the x-ray opacity of the anvil walls while preserving the essential hydrodynamic behavior of the original steel design. This required identifying a material and wall thickness that provided sufficient x-ray transmissivity through the anvil wall while maintaining adequate mechanical rigidity and impedance to support the internal shock reflections.

The transmission of the ESRF ID19 synchrotron source spectrum through materials within the assembly was evaluated using National Institute of Standards and Technology (NIST) mass attenuation coefficients.[30] Figure 3 shows the photon count as a function of energy for the unattenuated source spectrum and for both iron and aluminum at several thicknesses. A thickness of 1.0 mm of iron (used as an analog for steel) significantly reduces the photon flux. This corresponds to an anvil-wall thickness of approximately 0.5 mm since the x rays must traverse the wall both on entry to and exit from the amplifier. The result indicates that an exceptionally thin wall would be required for a steel anvil, and this material was, therefore, deemed unsuitable.

The attenuation of aluminum was also evaluated at a thickness of 37 mm, representative of the maximum penetration distance in the standard design. This configuration resulted in minimal x-ray transmission, indicating that a reduction in anvil-wall thickness was necessary even when using aluminum. It was found that

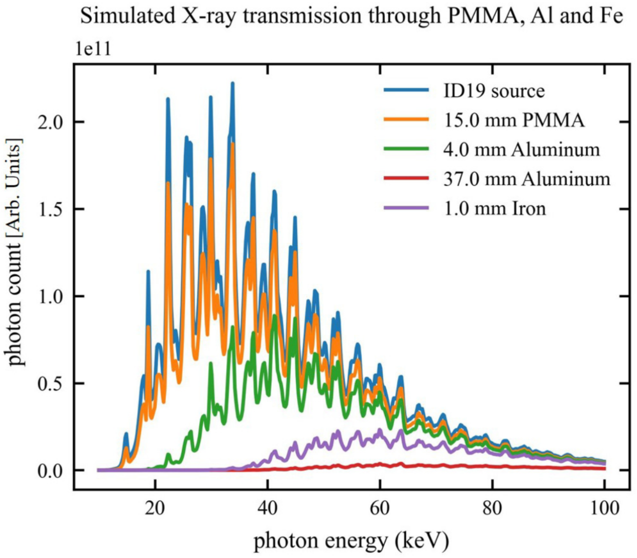

FIG. 3. Simulated transmission of the ESRF ID-19 x-ray spectrum through key materials in the amplifier assembly. The high attenuation associated with steel and full-thickness aluminum highlights the requirement for a reduced-thickness aluminum wall to allow effective x-ray phase-contrast imaging.

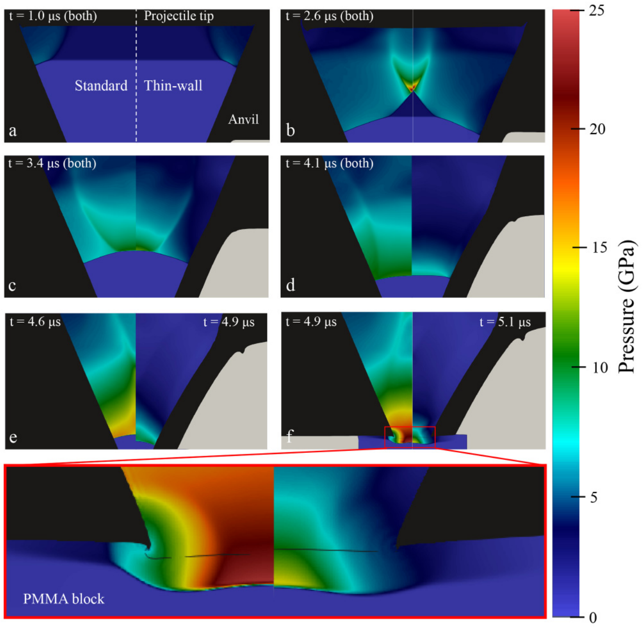

FIG. 4. Side-by-side comparison of the pressure field within the fill region of the standard (left) and thin-walled (right) 45° pressure amplifier. The pressure field shows the internal shock interactions, as outlined in Fig. 2. Shock dynamics remain similar between the two variants for the majority of the shock transit through the amplifier, with the largest difference being that the second Mach-stem convergence on-axis occurs slightly later in the thin-walled variant (e), and that there is a noticeable reduction in output pressure (f). Both designs produce a near planar shock at unload, with a higher pressure than that from the initial impact.

4.0 mm of aluminum (equivalent to 2.0 mm thick anvil walls) provided sufficient transmissivity to enable PCI measurements.

Also shown is the transmission through 15 mm of PMMA, used as an analog for the UV-cured resin fill (Dymax 6-621). PMMA exhibits relatively low attenuation across the ID19 spectrum and has a comparable density ($1.175\,\mathrm{g/cm^3}$) to the resin ($1.08\,\mathrm{g/cm^3}$), for which tabulated NIST data are unavailable.

To minimize energy loss through the anvil wall, and considering the field of view (FOV) of the PCI diagnostics, the wall thickness was reduced to 2.0 mm only in the lower portion of the amplifier, from just above the location of the first on-axis shock reflection to the outlet. Hydrodynamic simulations of these thin-walled aluminum designs showed that, although the outlet pressures were reduced relative to the full-thickness configurations, the essential internal shock dynamics were preserved, enabling experimental validation of the shock interactions within the amplifier. A comparison of the simulated pressure fields for the standard steel and thin-walled aluminum amplifier designs is shown in Fig. 4. The timing and position of both the first on-axis shock reflection (a) and (b) and the first anvil-wall reflection (c) and (d) remain similar in both configurations. Following reflection from the anvil walls (d) and (e), the shock dynamics begin to diverge slightly, with the second on-axis reflection (e) occurring marginally later in the thin-walled configuration. Importantly, this interaction still occurs prior to the shock unloading, resulting in the formation of an expanding Mach stem at the amplifier outlet.

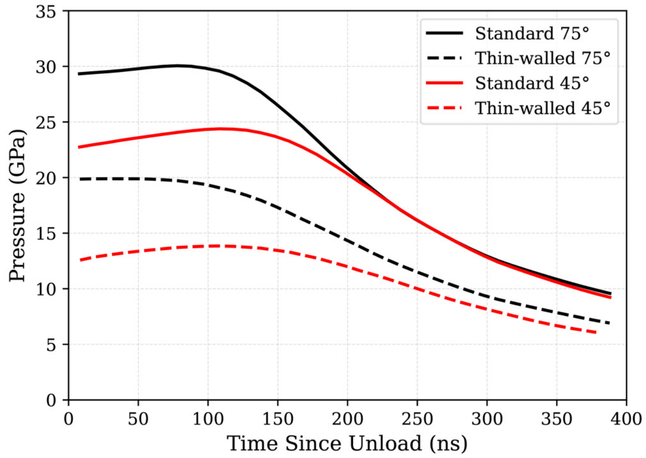

FIG. 5. Simulated amplifier unload shock pressure (into a PMMA sample) averaged over a radius of 0.25 mm, for standard and thin-walled variants of the 75° (black) and 45° (red), respectively. A discrepancy between standard and full thickness of ∼10 GPa is evident in both cases resulting from the energy lost due to the lower impedance aluminum and thinned wall section.

The differences in shock dynamics arise primarily from energy loss through the thinner aluminum walls, which leads to lower pressures at breakout. Figure 5 shows the on-axis shock-head pressure as a function of time following breakout into a PMMA block. The simulations indicate that the standard 45° and 75° designs produce peak pressures of approximately 25 and 30 GPa, respectively, whereas the corresponding thin-walled designs reach peak pressures of approximately 15 and 20 GPa. This represents a reduction of roughly 10 GPa attributable to the reduced wall thickness.

C. Summary of manufactured amplifier variants

Figure 6 shows the geometric parameters of the four designs, and the corresponding geometric and material parameters are summarized in Table I. The standard and thin-wall designs share identical cone geometry and resin fill, differing only in anvil material and wall thickness (316L stainless steel for the standard configuration and aluminum 6082 for the thin-walled variant).

III. EXPERIMENTAL VALIDATION

Experiments were performed on the 25 mm bore single-stage gas launcher located at the ESRF.[13] Ultrahigh speed (UHS) x-ray imaging was used to elucidate the internal shock dynamics of the amplifier and through a PMMA (9 mm diameter and 12 mm thick) sample bonded to its output. This method allowed for the determination of the shock-front dynamics in the amplifier and the sample, which allowed for comparison with our hydrodynamic simulations. Experiments were conducted using the 45° and 75°

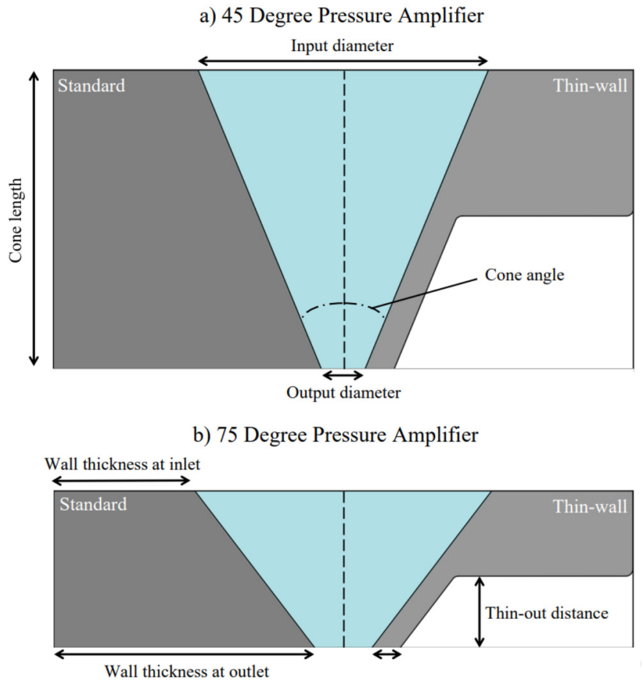

FIG. 6. Geometry of the standard (left) and thin-walled (right) pressure amplifier cone designs showing the key geometric parameters. (a) 45° pressure amplifier indicating the input diameter, output diameter, cone length, and cone angle. (b) 75° pressure amplifier highlighting the wall thickness at the inlet and outlet and the thin-out distance. The geometric and material parameters for the four designs are summarized in Table I.

variants. Complementary experiments were performed using the single stage gas launcher facility at the University of Oxford, which is similar in specifications to the ESRF SSGG.[13] In these experiments, PDV was used to track the velocity history of shocked samples allowing for the pressure conditions to be determined. Aluminum foils with lithium fluoride windows as well as iron and copper free-standing foils were tested. In both experimental campaigns, polycarbonate sabots with aluminum tips were used, with flyer velocities consistently reaching approximately 800 m/s.

A. Ultrahigh speed (UHS) x-ray imaging (XRI)

Ultrahigh speed (UHS) x-ray imaging (XRI) is a technique used for in *situ* radiography of ultrafast (sub-microsecond) processes. The technique has been implemented successfully at the ESRF beamline ID-19[13,18] to achieve effective frame rates (fps) of over 5 Mfps. X rays are emitted in evenly spaced pulses from electron bunches circulating in the synchrotron storage ring, driven by the radio frequency power supply.[31] Each bunch has a minimum duration of ∼100 ps with the inter-bunch time depending on the mode of operation selected. This work utilized a 16-bunch mode, which gave an inter-bunch timing of 176 ns.[32] The multiplexed camera configuration for maximizing frame rate, utilizing three Shimadzu Hyper-Vision HPV-X2 ultrafast imaging cameras, has been outlined in previous work.[18] The HPV-X2 while in an adjustable frame rate mode has a minimum inter-frame time of 500 ns (2 Mfps), adjustable in 10 ns steps. Synchronization between the x-ray pulse train and the inter-frame camera timing is achieved by using three HPV-X2 cameras triggered in sequence with 530 ns inter-frame times, closely matched to the temporal separation between 3 bunches (528 ns). An effective frame rate of 5.68 Mfps is then achieved by combining the three separate image sets in post-processing. Figure 7 illustrates the experimental setup, which used a single 250 μm (Cerium-doped Lutetium–Yttrium Oxyorthosilicate) LYSO:Ce scintillator.[33] Camera 1 imaged the upstream optical emission from the scintillator, while Cameras 2 and 3 imaged the downrange emission via a 50:50 pellicle beam-splitter arrangement, enabling indirect x-ray imaging of the impact region across all three Shimadzu cameras. After passing through the PMMA sample, the pulsed x-ray beam was converted to optical emission by the scintillator and relayed to the cameras through a combination of various beam splitters and mirrors. The effective x-ray FOV on the cameras was approximately 12 × 8 mm, as indicated by the purple box in Fig. 7(b). Cameras were synchronized to projectile impact via light gates and various triggers in phase with the x-ray bunches delivered to ID-19 beamline. Further information, such as timing diagrams, scintillator absorption and emission spectra, and x-ray spectra, and a more detailed explanation of the multiplexed camera system implementation with the synchrotron are outlined in previous work.[18]

B. Phase-contrast imaging for shock propagation imaging

X-ray phase-contrast imaging (PCI)[34] is a diagnostic technique that enhances the visibility of shock fronts as well as static objects by detecting variations in the phase shift of x rays as they pass through materials with differing densities. Unlike conventional x-ray absorption imaging, which relies on attenuation, PCI is sensitive to density gradients, making it particularly effective for imaging low-Z materials and transparent media under dynamic loading without the need for contrast agents. Figure 7(b) illustrates the specific setup used with the single-stage gas launcher at the ESRF, where PMMA samples were placed on the output of the amplifier to allow imaging of the shock front as it exited the conical amplifier. The thin-walled (low x-ray attenuation) amplifier variants were fielded to enable x-ray phase-contrast imaging of the interior of the amplifier. The resulting x-ray phase-contrast images enabled detailed assessment of shock dynamics by providing a visual representation of shock evolution. In addition to the aluminum variants used for PCI, steel amplifiers were also fielded in the experimental campaign. These steel designs are highly attenuating to x rays but were included to verify that the shock structures observed at the amplifier output, particularly the formation and expansion of the Mach stem, were consistent with those produced by the thin-walled variant. Comparison of the PCI results with corresponding simulations confirmed that both the aluminum and steel amplifiers exhibited the same qualitative shock dynamics at breakout, with the former providing access to the interior shock dynamics.

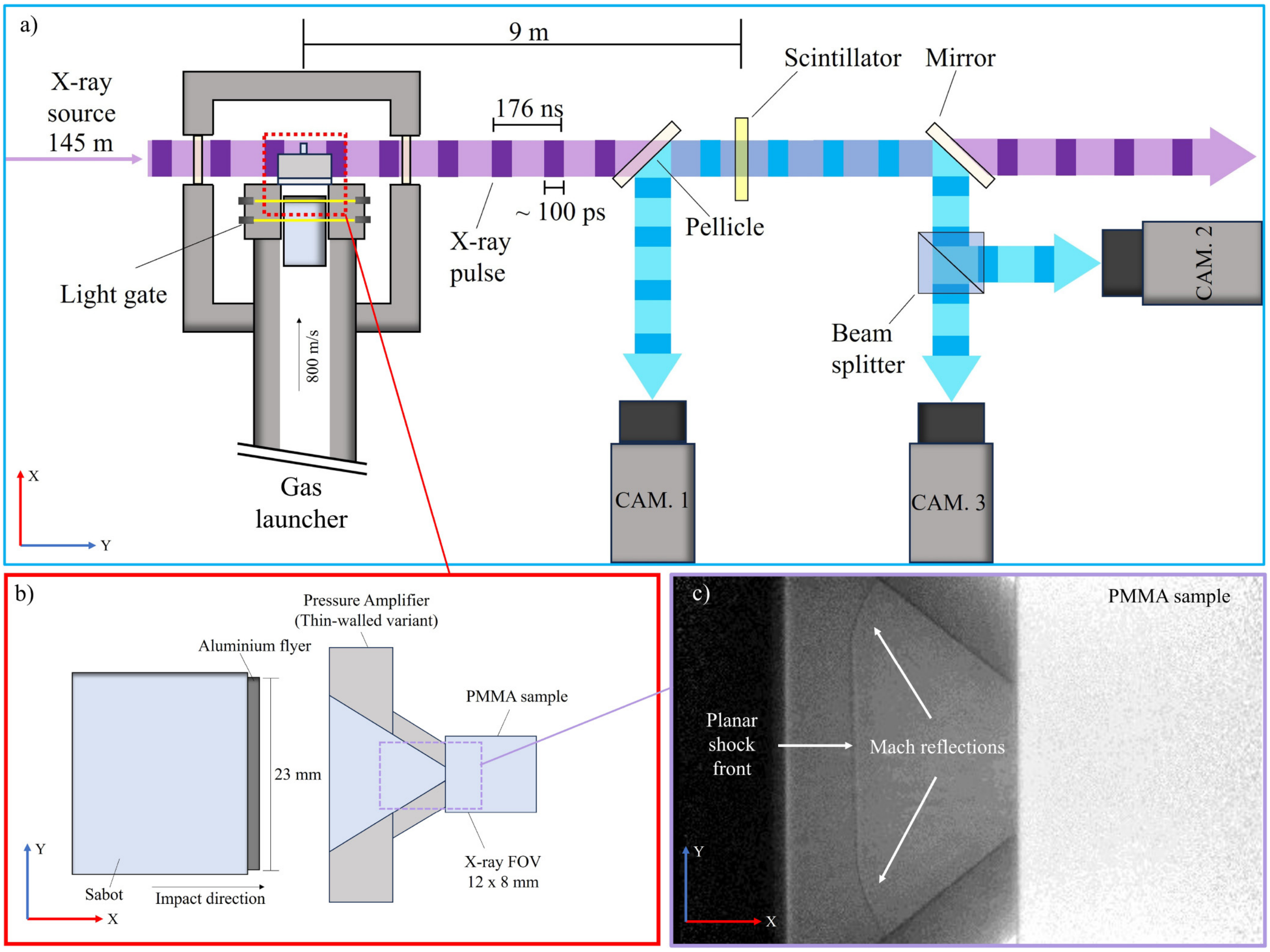

FIG. 7. Experimental setup used for impact studies at the ESRF. (a) Schematic of the ultrahigh-speed x-ray imaging (UHS XRI) setup, including the beam-line, cameras, and single-stage gas launcher. The setup incorporates a single pellicle beam splitter, a cube beam splitter, and a 250 μm (Cerium-doped Lutetium–Yttrium Oxyorthosilicate) LYSO:Ce scintillator with camera 1 imaging the up range emission and cameras 2 and 3 imaging the downrange emission. The amplifiers were impacted by an aluminum flyer accelerated to 800 m/s. With the subsequent progression of the shock through the latter half of the amplifier and its exit into PMMA, samples were examined *in situ* using single bunch (100 ps) hard x-ray pulses separated by 176 ns. The x-ray beam is indicated in purple with the pulses in dark purple. The optical light incident on the cameras is indicated in blue, with the optical pulses corresponding to the x-ray pulses in dark blue. (b) A schematic of the impact region at ESRF [red dashed box in (a)], showing the aluminum flyer and the thin-walled pressure amplifier, (c) Phase-contrast images of shock propagation through a 75° cone angle thin-walled amplifier variant and a PMMA sample. With the purple dashed box [in (b)] outlining the x-ray field of view.

Although PCI frames can, in principle, be used to estimate shock velocity and infer pressure via Rankine–Hugoniot relations, extracting velocity from these frames introduces large uncertainties due to the spatial resolution. Furthermore, while UHS-XRI achieves effective frame rates exceeding 5 Mfps, the inter-frame time of 176 ns was still substantially longer than the timescale of breakout dynamics (tens of ns), meaning the peak pressure at release could not be captured. Therefore, because of the discrete nature of the imaging, the inferred pressures would represent averages between two frames and offer little practical value. To obtain accurate measurements of amplifier output pressures and quantify the pressure enhancement, complementary experiments employing PDV were conducted at the University of Oxford.

C. Photon Doppler velocimetry for interface velocity measurement

The PDV system employed used two narrow-linewidth (<700 Hz), single-frequency CW fiber lasers operating near 1550 nm, enabling a tunable zero velocity frequency shift.

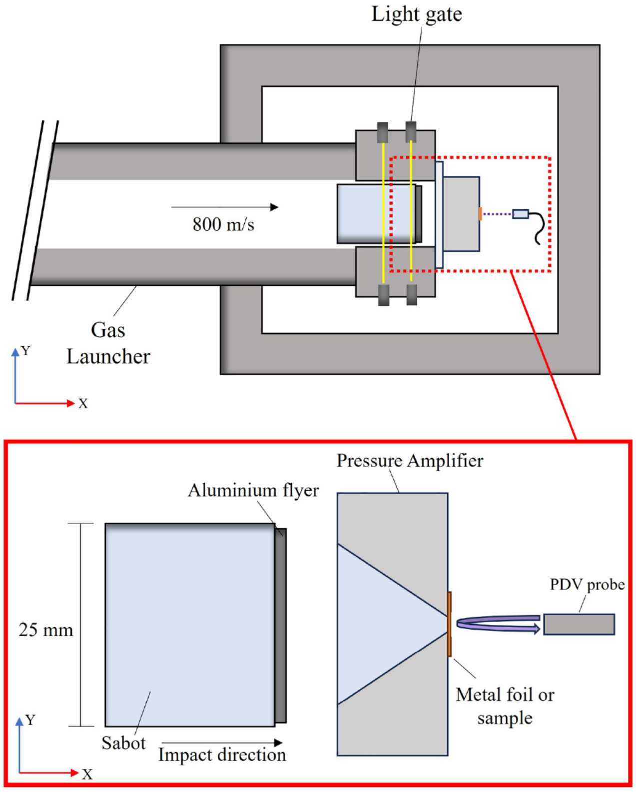

FIG. 8. Schematic of the experimental setup used at the University of Oxford, single-stage gas launcher muzzle, and impact chamber with light gate shown along with the target hardware. Zoomed in target area highlighted in red, including the pressure amplifier, aluminum tipped projectile, foil, or sample as well as a single collimating probe used to record the interface of shocked samples.

Experiments were typically conducted using a frequency shift of 1 GHz to improve temporal resolution. Signals were detected using a Thorlabs DET08CFC/M InGaAs biased detector and recorded on a LeCroy WaveMaster 808ZiB oscilloscope with an 8 GHz bandwidth and a 40 GS/s sampling rate, enabling high temporal and spatial resolution. Further details on the system configuration and methodology can be found in previous work.[35]

Figure 8 illustrates the experimental setup used at the SSGG at the University of Oxford. A single-mode optical fiber coupled with a Thorlabs 1550 nm Single Mode graded-index fiber collimator produced a collimated beam approximately 0.5 mm in diameter. Time-resolved interferometric velocimetry, such as VISAR and PDV, are widely used to measure free-surface velocity histories in shock compression experiments and relate them to Hugoniot states for pressure determination. The quasi-steady (plateau) portion of the free-surface velocity trace prior to release-induced acceleration provides an objective measure of the peak shock state, with the corresponding pressure calculated via Rankine–Hugoniot analysis.[36]

For interface velocity measurements in samples with confining windows, the peak pressure state is taken as the constant hold-time velocity immediately following release into the sample. This approach is consistent with standard dynamic compression diagnostics, in which time-resolved interface velocity histories are used to infer shock states via impedance matching and Hugoniot analysis.[37,38] A detailed discussion of the path from the measured velocity to the sample pressure states as well as the Hugoniot relations and parameters used is outlined further in Appendixes B–D.

For a metallic sample, the free-surface velocity is typically approximated as twice the particle velocity u_p, based on momentum conservation at a stress-free boundary.[39] This relationship can deviate in the presence of material phase transitions; however, in the relatively low-pressure regime examined in this study, such deviations are expected to be small and have a negligible effect on the inferred pressure values.[40] This analysis also assumes that the release isentrope does not differ significantly from the Hugoniot, an approximation that is again valid at the low pressures considered here.

An amplification ratio (AR) is outlined here, which is used to quantify the performance of the amplifiers, presented in Sec. IV, being defined as

$$\mathrm{AR} = \frac{P_{\mathrm{out}}}{P_{\mathrm{DI}}}, \tag{1}$$

where P_{out} is the peak sample pressure and P_{DI} is defined as the direct-impact pressure imparted into the amplifier by the projectile. In this work, P_{DI} is the direct-impact pressure produced by planar impact of an aluminum flyer at the measured projectile velocity (approximately 800 m/s), impedance-matched to the Hugoniot[41] of the sample (LiF, Cu, or Fe) to determine the corresponding baseline direct-impact pressure used for calculation of the amplification ratio. (Further discussion is provided in Appendix E.)

With the experimental methods established, Sec. IV presents results from both UHS XRI alongside simulations and supporting PDV measurements to characterize the pressure amplifier performance.

IV. RESULTS

A. Phase-contrast imaging of shock dynamics

A total of six shots were performed at the ESRF, which used x-ray PCI to diagnose shock dynamics within the amplifier and the PMMA sample bonded to the outlet of the amplifier. These shots are summarized in Table II. Four experiments were conducted using the thin-walled amplifier variants, while two experiments employed the standard steel configuration. For the standard configuration, the amplifier was positioned such that the PCI FOV was primarily focused on the unload block, as x-ray transmission through the anvil walls was not possible.

1. Qualitative comparison of shock morphology

a. 75° amplifier variant. Figure 9 shows PCI frames corresponding to shot 2 (75° thin-walled), illustrating the propagation of the shock imparted by the projectile impact through the amplifier and into the PMMA sample. In Fig. 9(a), interactions between the planar shock front (originating from projectile impact) and the

TABLE II. Summary of experiments performed on the single-stage gas launcher at the ESRF. Projectile velocities were measured with an uncertainty of ±10 m/s for all shots.

Shot ID	Angle (°)	Variant	Anvil material	Projectile velocity (m/s)
1	45	Thin-wall	Aluminum	804
2	75	Thin-wall	Aluminum	795
3	75	Standard	Steel	806
4	45	Standard	Steel	773
5	75	Thin-wall	Aluminum	790
6	45	Thin-wall	Aluminum	793

anvil walls initiate Mach reflections (label 1). Figure 9(b) highlights the progression of these reflections toward the central axis (label 2), with Fig. 9(c) showing the formation of the Mach stem (label 3). In the subsequent frames [Figs. 9(d)–9(g)], the Mach stem expands to fill the amplifier output as the shock releases into the PMMA sample.

Figure 10 presents a side-by-side comparison of the experimental PCI results for shot 5 (75° thin-walled amplifier) and corresponding snapshots from the 2D hydrodynamic simulation. Twelve frames are shown [Figs. 10(a)–10(l)], corresponding to the final ~1.3 μs of the shock propagating through the amplifier prior to unloading into the PMMA sample. The simulation field was exported with 10 ns temporal resolution, while the PCI frames are separated by 176 ns. Simulation snapshots were selected to align with the observed shock position in the PCI images to facilitate a qualitative comparison of the shock shape and propagation. As such, the frames do not necessarily correspond to identical absolute times; quantitative comparisons of shock positions as a function of time, for all shots, are presented separately in Sec. IV A 2.

Figure 10(a) shows the planar shock front, which had already traveled through the "thick" portion of the amplifier body before entering the PCI field of view, so interactions with the anvil walls had already begun. Some features behind the shock front that can be seen converging onto the central axis in simulated frames are not resolved by the PCI due to the resolvable density-gradient cutoff. Figures 10(a)–10(e) show the planar shock front produced by the projectile impact continuing to propagate forward, while Mach reflections can be seen traveling radially inward after interacting with the anvil wall. Figures 10(f) and 10(g) show the Mach reflections coalescing with the planar shock front along the central axis, and Fig. 10(h) shows the formed Mach stem just before it fills the amplifier output. The subsequent frames [Figs. 10(i)–10(l)] show the output shock entering the PMMA sample, initially convex, becoming briefly planar, before finally turning concave. The simulations accurately reproduce the experimentally observed shock front morphology at several stages of propagation through the amplifier and during subsequent unloading.

b. 45° amplifier variant. Figure 11 presents a side-by-side comparison of the experimental PCI results for shot 1 (45° thin-walled amplifier) and the corresponding snapshots from the 2D hydrodynamic simulation. Nine frames are shown [Figs. 11(a)–11(i)] corresponding to the final ~2 μs of the shock traveling through the amplifier before exiting into the PMMA sample. Similarly to comparison for the 75° variant (Fig. 10), snapshots from the simulation were selected to align with the experimentally observed shock position. Figures 11(a)–11(f) show the continuation of the shock front, having traveled approximately halfway through the amplifier body with one Mach stem formation already having occurred before entering the PCI FOV as highlighted previously (Fig. 2). Figures 11(g)–11(i) show the secondary Mach stem formation prior to filling the output of the amplifier and releasing into the PMMA sample. Although the release into the PMMA sample was captured by PCI, it is not shown in Fig. 11 because the weaker unload shock produced a density gradient near the PCI detection limit, making the shock difficult to resolve.

2. Quantitative comparison of shock position-time evolution

To further compare the hydrodynamic simulations with the PCI data, Fig. 12 presents the shock-front position extracted from PCI as a function of time, together with the corresponding simulated trajectories for both thin-walled and standard amplifier geometries [75° and 45°, Figs. 12(a)–12(d), respectively]. The

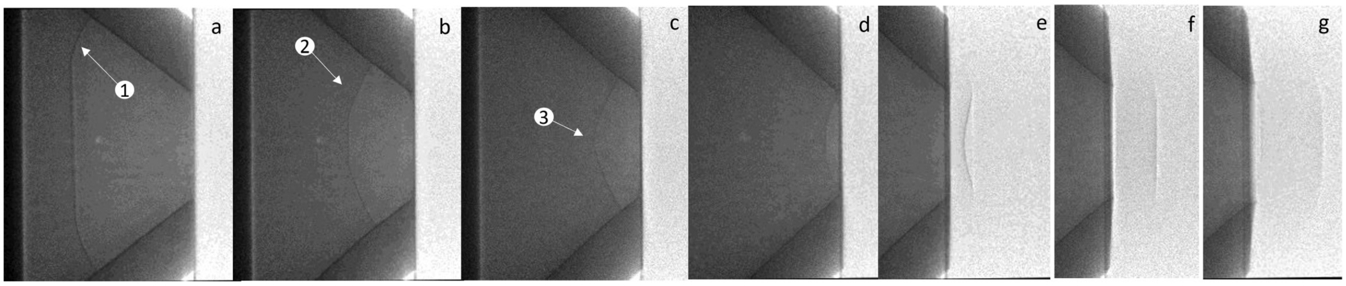

FIG. 9. X-ray PCI frames corresponding to shot 2 (Table II). Shown is the propagation of the shock imparted by the projectile impact through the amplifier into a PMMA sample. Label 1 highlights the interactions between the planar shock front and the anvil, which cause Mach reflections. Label 2 highlights the Mach reflections progression toward the central axis. Label 3 highlights the formation of the Mach stem, which in the subsequent frames (d)–(g) expand to fill the output as the shock releases into the PMMA sample.

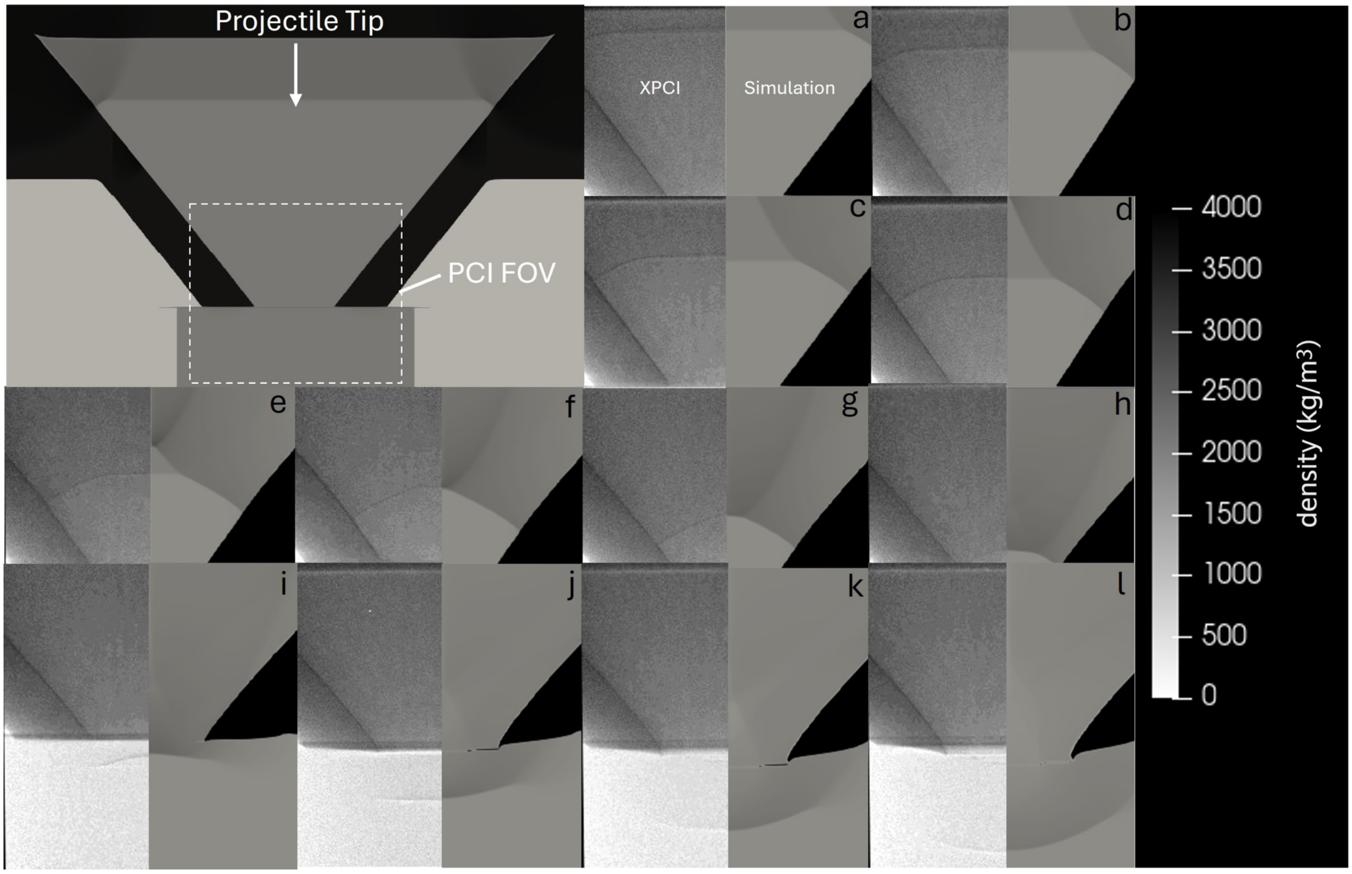

FIG. 10. Evolution of shock through the 75° thin-walled amplifier (shot 2). (left) Shows the phase-contrast images (PCIs) from the ESRF ID-19 beamline with separations of 176 ns between frames. (right) Simulated B2 snapshots showing shock-front evolution through the amplifier with density as the field, which is directly comparable to shock fronts visible in the PCI frames. Features present behind the shock front in the simulations are not visible in the PCI frames due to the resolvable density cutoff of the imaging. Mach stem formation occurs between frames d and e with the created Mach stem expanding in the following frames (f)–(h) before exiting into the PMMA sample (i)–(l).

shock-front position in the experimental data was determined from the PCI images using axial line-outs through the central region of the shock front, representing a lateral average over ± 0.25 mm about the amplifier z-axis. For both geometries, the simulated and measured shock front trajectories were temporally and spatially aligned by anchoring $t = 0$ at the first emergence of a shock in the PCI. All positions are measured relative to the outlet of the amplifier ($z = 0$), with positive z defined in the direction of shock propagation. In all cases, the PCI data points are shown with vertically propagated uncertainty bars, which account for the pixel-level uncertainty in localizing the shock front, the fiducial-reference uncertainty, and the finite accuracy of the pixel-to-distance calibration. The resulting positional uncertainty contains both a constant component arising from the intrinsic precision with which the shock edge can be located in the raw PCI images—and a distance dependent contribution associated with the mm-per-pixel calibration error. In the standard (steel) variants [Figs. 12(c) and 12(d)], the simulated shock trajectories from amplifier exit through the PMMA sample agree with the PCI measurements to well within the experimental positional uncertainty over the entire transit. For the thin-walled variants [Figs. 12(a) and 12(b)], the 75° case shows similarly strong agreement with the simulations across the shock trajectory, from propagation within the amplifier to release into the PMMA sample. In contrast, the 4° thin-walled configuration exhibits a modest divergence at later times, with the PCI measurements tending to lie slightly above the simulated trajectory, indicating that the simulation overpredicts the shock velocity in this case. This increased divergence may reflect limitations in the modeling of the more complex sequence of shock and wall interactions in the 45° configuration.

Overall, the experimental and simulated trajectories presented in Figs. 10–12 show good agreement throughout propagation and breakout into the PMMA sample, indicating that the hydrodynamic model captures the key features of the shock dynamics, including

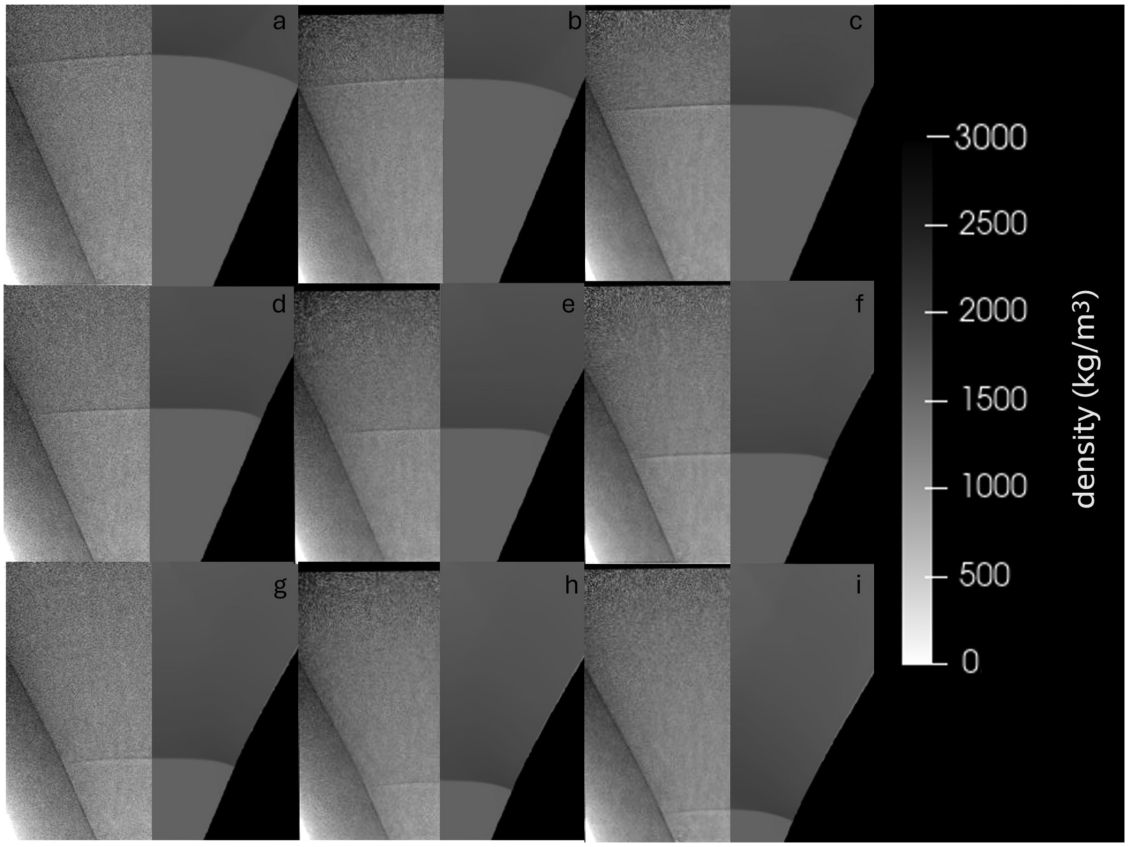

FIG. 11. Evolution of shock through a 45° thin-walled amplifier (shot 1). (left) Shows the phase-contrast images (PCI) from the ESRF ID-19 beamline with separations of 176 ns between frames. (Right) Simulated B2 snapshots showing shock-front evolution through the amplifier with density as the field, which is directly comparable to shock fronts visible in the PCI frames. Frames (a)–(f) show the continuation of the shock front through the amplifier after the first Mach stem formation as highlighted previously in Fig. 2. The second Mach stem formation occurs between frames (g) and (i), with the release into the PMMA sample not shown here as the reduced output pressure compared to the 75° variant results in a shock front that is difficult to resolve.

the timing of Mach reflections, Mach-stem growth, and subsequent release. This level of agreement provides support for the ability of the B2 code to represent complex shock interactions in this configuration and suggests that such simulations can be used to inform the design of related amplifier geometries. In particular, this capability may enable the optimization of amplifier configurations to achieve desired outputs for specific applications, such as improved planarity and extended hold times.

B. Photonic Doppler velocimetry of shocked samples

A series of seven experiments were conducted using the single-stage gas launcher located at the University of Oxford, employing PDV to characterize the output conditions of both aluminum and steel pressure amplifiers. While thin-walled amplifiers were essential for PCI measurements, the majority of PDV experiments employed the steel variants. These steel designs provide a higher pressure amplification as the thicker, higher-impedance anvil reduces energy loss through the wall. Pressure states achieved in each material along with the corresponding amplification ratio (AR) from these experiments using Cu, Al/LiF, and Fe samples are summarized in Table III. We note the typical uncertainties associated with the velocity measurements. Depending on the sample configuration, the PDV signal corresponds either to the free-surface velocity of a metallic foil or to the interface velocity at an Al/LiF window. For both free-surface and interface velocity measurements, the dominant contributions to the total uncertainty arise from the instrumental response and from the interpretation of quasi-steady regions in the velocity histories. The instrumental contribution set by the oscilloscope sampling rate, detector bandwidth, and signal processing is estimated to be approximately $\pm 20\,\mathrm{m/s}$.

The interpretation uncertainty is quantified by evaluating the variation of the measured velocity within the nominal plateau region. Specifically, we take the difference between the minimum and maximum velocities over the interval identified as quasi-steady, which typically contributes an additional $\pm 10 - 60\,\mathrm{m/s}$ depending on signal quality and sample configuration. This velocity uncertainty is further propagated into the calculation of the peak

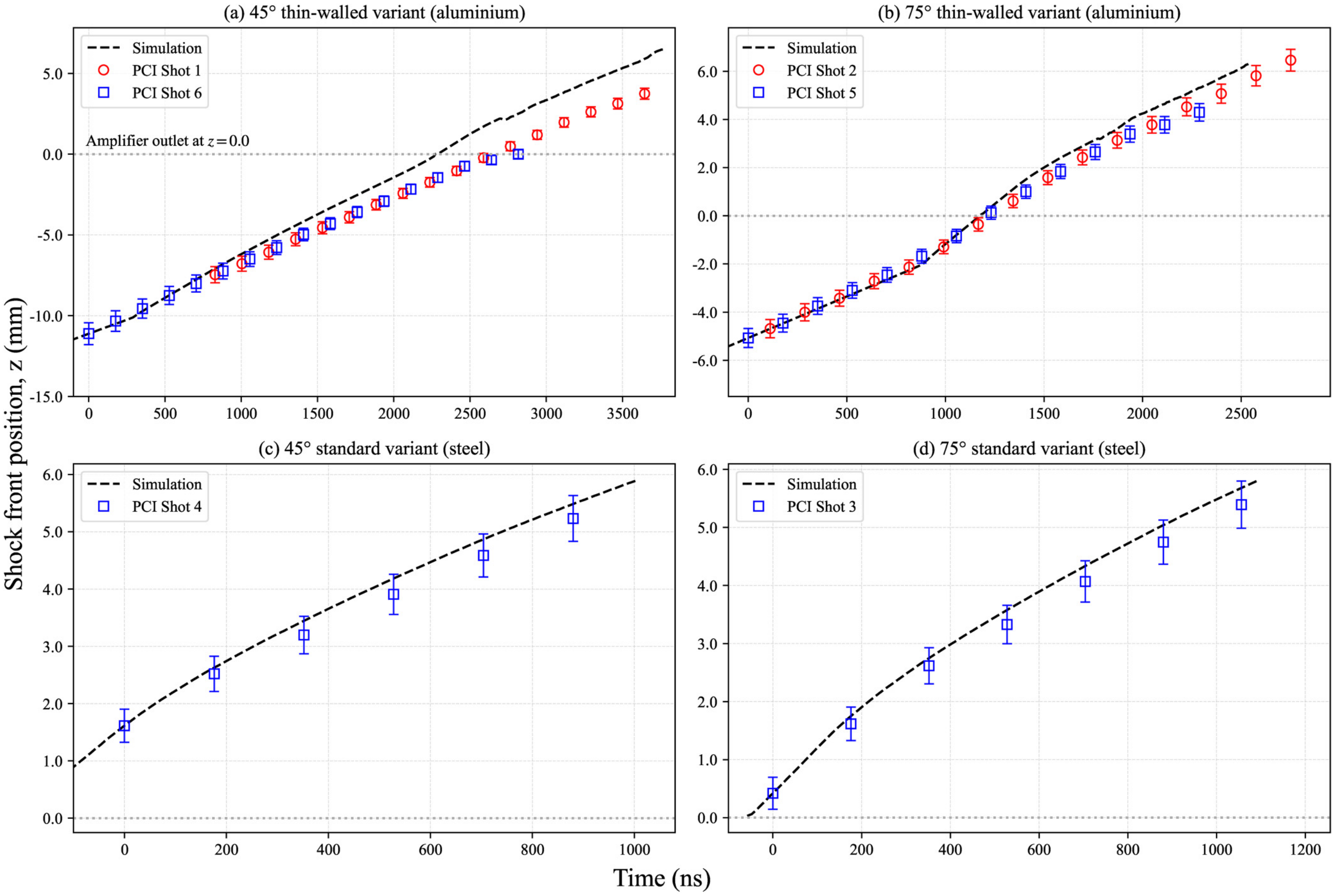

FIG. 12. Comparison of simulated and PCI-measured shock positions within the amplifier and in the (PMMA) unload block for the six PCI shots described in Table II. The shock position is plotted as a function of time, where z is the axial position of the shock averaged over a radial region of ± 0.25 mm from the z-axis, in both the simulation and the PCI measurements. The simulation time has been shifted such that $t = 0$ corresponds to the first PCI measurement, and the shock occupies the same axial position in both datasets at that time. All positions are measured relative to the outlet of the amplifier ($z = 0$), with positive z defined in the direction of shock propagation.

TABLE III. Summary of experiments performed on the single-stage gas launcher at the University of Oxford. Pressure values calculated using material-specific Hugoniot relations. The particle velocity inferred using the particle velocity/free-surface velocity relation where applicable.

Shot ID	Angle (°) (material)	Sample material	Sample thickness	Projectile velocity (m/s)	Particle velocity (m/s)	Peak sample pressure (GPa)	Amplification ratio AR = $P_{\text{out}}/P_{\text{DI}}$
1	75 (Al)	LiF	3 mm	790 ± 8	854 ± 33	14.28 ± 0.65	2.32 ± 0.11
2	75 (S)	Cu	75 μm	816 ± 10	800 ± 29	36.51 ± 1.63	3.99 ± 0.18
3	75 (S)	LiF	3 mm	801 ± 7	1410 ± 40	26.37 ± 0.96	4.28 ± 0.16
4	45 (S)	Fe	250 μm	799 ± 7	631 ± 40	24.5 ± 2.9	2.67 ± 0.25
5	45 (S)	Cu	75 μm	793 ± 12	546 ± 23	23.07 ± 1.13	2.52 ± 0.12
6	75 (S)	Fe	500 μm	787 ± 16	960 ± 67	39.9 ± 4.1	4.36 ± 0.39
7	75 (S)	LiF	3 mm	784 ± 7	1356 ± 47	25.10 ± 1.09	4.07 ± 0.18

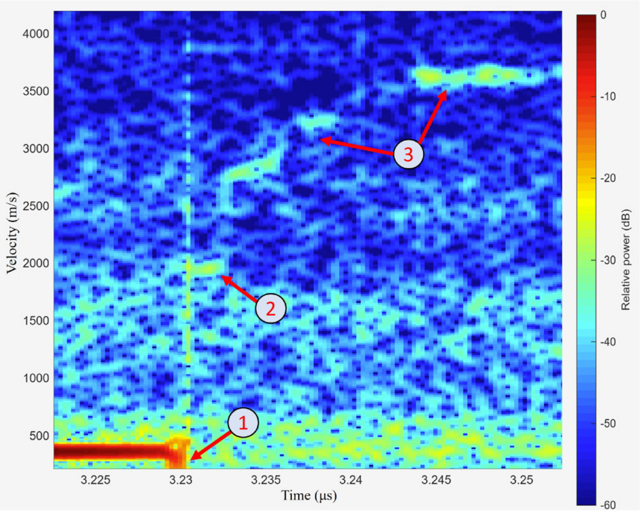

FIG. 13. Downshifted PDV spectrogram of the free-surface velocity from a 75 μm copper foil bonded to a steel 75° amplifier variant. A sharp breakout feature (label 1) marks shock emergence at the rear surface, reaching a free-surface velocity of approximately 1600 m/s, 36.5 ± 1.6 GPa. This is followed by a 20 ns plateau (label 2) associated with reverberation and the peak stress state within the sample. Subsequently, the foil undergoes continued acceleration (label 3), indicating residual drive from the amplifier system.

pressure states via Hugoniot relations discussed previously, with detailed discussion of full uncertainty propagation outlined in Appendixes A and F.

1. Copper (Cu)

Figure 13 shows a downshifted PDV spectrogram corresponding to the measurement of the free-surface velocity of a 75 μm copper foil bonded to the output of a steel 75° amplifier variant. A sharp breakout feature marks shock emergence at the rear surface, where the free-surface velocity reaches approximately 1600 m/s, corresponding to a peak pressure of 36.5 ± 1.63 GPa using the acoustic approximation $U_{fs} = 2u_p$[40] along with Hugoniot relations as previously discussed. Following breakout, a steady 20 ns velocity plateau is observed, associated with reverberation and the peak stress state within the sample. After this plateau, the foil undergoes continued acceleration, and the finite thickness of the Cu foil introduces reverberations that modify the measured velocity profile.

A second shot using a 45° steel amplifier and a 75 μm Cu sample demonstrated a sharp breakout with a peak free-surface velocity of 1100 m/s followed by a plateau in the velocity, which holds for approximately 30 ns taken as the steady region corresponding to the peak pressure state. The velocity plateau corresponds to a pressure of 23 ± 1.13 GPa. This represents a 2.5-fold pressure increase relative to direct impact.

2. Lithium fluoride (LiF)

Experiments were conducted using LiF windows backed with a thin aluminum foil (3 μm) to provide a reflective interface.

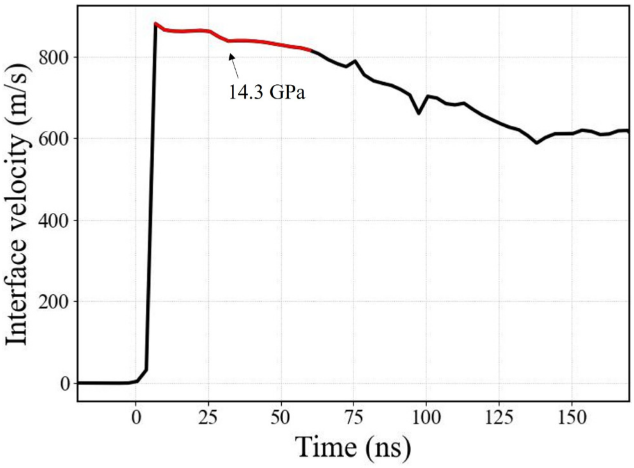

FIG. 14. Output of a 75° aluminum amplifier into a lithium fluoride (LiF) window backed with a thin aluminum layer, recorded using PDV (Shot 1). The Al/LiF interface reaches a peak pressure of 14.28 GPa ($u_p = 854$ m/s), which is maintained for approximately 50 ns (highlighted in red) before the shock decays as it continues into the LiF window.

Measured velocities were corrected for the refractive index of LiF using

$$u = 0.7895\, u_*^{0.9918}, \tag{2}$$

where u_* is the apparent velocity, consistent with literature values for LiF at 1550 nm.[42]

Figure 14 highlights the measured velocity trace for the thin-walled 75° amplifier used with a LiF sample (shot 1 Table III). The Al/LiF interface reached a peak velocity of 854 m/s, which was held for approximately 50 ns. This quasi-steady region in the velocity trace (highlighted in red in Fig. 14) is taken as the peak pressure state, corresponding to 14.28 ± 0.65 GPa.

Shots 3 and 7 (Table III) employed 75° steel amplifiers again with LiF samples. Peak interface velocities of 1400 and 1350 m/s were measured, corresponding to pressures of 26.37 ± 0.96 and 25.1 ± 1.09 GPa, respectively. The PDV signals were lost shortly after shock breakout; consequently, only ≤10 ns of the quasisteady plateau region corresponding to the peak pressure state could be determined, and the subsequent interface velocity within the LiF sample could not be resolved.

A direct comparison between the pressure states achieved using the standard and thin-walled amplifier variants is particularly noteworthy. Relative to shots 3 and 7, shot 1 exhibits reductions in the peak sample pressure of 12.02 and 10.28 GPa, respectively. When accounting for experimental uncertainty and small variations in the projectile velocity (which are known to influence achievable pressure in amplifier geometries[22]), the discrepancy between the thin-walled and standard amplifier configurations is consistent with the expected difference predicted by simulations (∼10 GPa). This agreement provides further validation of the B2 hydrocode's fidelity in modeling the shock dynamics in the presented geometry.

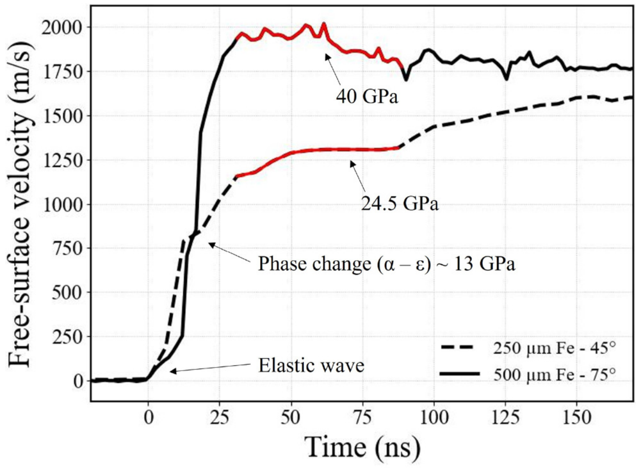

FIG. 15. Output from 75° and 45° steel amplifiers into 250 μm (dashed) and 500 μm (solid) thick iron foil samples, respectively. An elastic wave is present in both traces up to $u_p = 125$ m/s as well as the $\alpha \rightarrow \epsilon$ phase transition present at $u_p = 350$ m/s. Velocity plateaus (highlighted in red) at 1300 and 1950 m/s, existing for approximately 50 ns in the 250 and 500 μm samples, respectively, correspond to peak pressure states of 24 and 39 GPa.

3. α–ϵ phase change in iron

Iron is the archetypal system for studying phase transformations under shock compression. Bancroft *et al.* first reported the experimental observation of a polymorphic transition in Fe occurring at 13 GPa.[43] Subsequent static compression measurements[44–46] identified this polymorphic transition as the alpha (body centered cubic) to epsilon (hexagonal close packed) transformation, which has since been extensively studied.[47,48]

Figure 15 presents PDV free surface velocity histories for experiments performed using the steel 75° and 45° amplifier variants driving shocks into 250 and 500 μm iron foils. The free-surface velocity U_{fs} in iron is approximately $1.97u_p$.[47] The traces exhibit a distinct initial elastic wave, visible up to approximately 4 GPa ($u_p \sim 125$ m/s), corresponding to the Hugoniot elastic limit (HEL) of iron.[21] This is followed by a sharp increase in the velocity that marks the onset of plastic deformation and then a shoulder in the wave profile that marks the $\alpha \rightarrow \epsilon$ phase transition, observed at 13 ± 1.8 GPa ($u_p \sim 330 \pm 37$ m/s) for the 500 μm sample and transition at 14.5 ± 2 GPa for the 250 μm sample ($u_p \sim 364 \pm 40$ m/s). This variation in transition pressure is consistent with the trend reported by Smith *et al.*,[48] which shows that the onset pressure of the $\alpha \rightarrow \epsilon$ phase transition in iron increases with decreasing sample thickness. Measured velocity plateaus of 631 and 960 m/s, which persist for approximately 50 ns (highlighted red in Fig. 15), were observed for the 45° and 75° amplifier variants, respectively, taken as the peak pressure states. Sample pressures were calculated using the Rankine–Hugoniot conservation equations in a reshock form,[49] employing separate linear U_s–u_p relations for the α and ϵ phases to account for the phase transition.[21,50] Using this approach, the measured velocities correspond to peak pressures of 24.5 ± 2.9 and 39.9 ± 4.1 GPa.

Figure 16 places the pressure states achieved in the samples using the various amplifier configurations in context by plotting the pressure states against the representative P–u_p Hugoniots. For comparison, the reflected Al Hugoniots corresponding to $u_p = 0.4$ and 0.8 km/s are also shown, with their intersections with the sample Hugoniots indicating the pressures achievable through direct impacts at projectile velocities of 800 and 1600 m/s. These comparisons highlight that the amplifier geometry dramatically expands the accessible pressure range of a single-stage gas launcher. Notably, the 75° steel variant achieves a maximum amplification ratio (AR) of 4.3 in LiF and Fe—exceeding even the pressures from a direct 1.6 km/s impact despite using only a 0.8 km/s projectile. Even relative to a 1600 m/s impact, the amplifiers retain an AR of 1.95, underscoring the substantial performance enhancement they provide.

V. DISCUSSION

We have shown, through a side-by-side comparison of two-dimensional hydrodynamic simulations with UHS XRI, together with measurements of peak output pressures using PDV, that pressure amplifiers can substantially enhance the pressures achievable using single-stage gas launchers. The observed amplification ratios of up to 4.3 arise from geometric shock convergence and Mach-stem formation within the conical geometry, with the 45° and 75° variants differing primarily in the number and timing of these interactions. The choice of wall material and thickness also influences performance: steel-walled designs provide higher amplification due to their higher mechanical impedance, whereas the aluminum design sacrifices some performance to enable x-ray access while preserving the essential shock dynamics.

The amplifier design in this work shares similarities with configurations previously investigated using two-stage light gas guns, such as those reported by Gorman *et al.*[22] In that work, a multilayered amplifier was validated using the STAR facility at Sandia National Laboratories, where a projectile accelerated to 6.5 km/s generated output pressures of 1.07 TPa over a planar region of 1 mm with a hold time of 20 ns in a quartz sample.

The level of agreement observed between simulations and experiments in the present study provides support for the use of the B2 code in capturing the dominant features of shock amplification in these geometries. As such, the simulations offer a useful tool for exploring design variations and guiding the optimization of amplifier configurations, including geometric parameters, material selection, and the incorporation of additional features, such as layered fills.

More broadly, these results highlight the versatility of pressure amplifiers in generating a wide range of output pressures, from tens of gigapascals to multi-terapascal levels, depending on the driver system. While the current experiments were conducted at projectile velocities of only 800 m/s, the amplifier geometry demonstrated here could reach significantly higher pressures at increased impact speeds, which are accessible on more advanced single-stage platforms. This capability further expands the applicability of pressure amplifiers in dynamic materials research. Continued refinement of amplifier designs, including the use of higher-impedance anvil materials, modified geometries, and more complex internal structures, may enable further increases in achievable pressure and improvements in shock planarity.

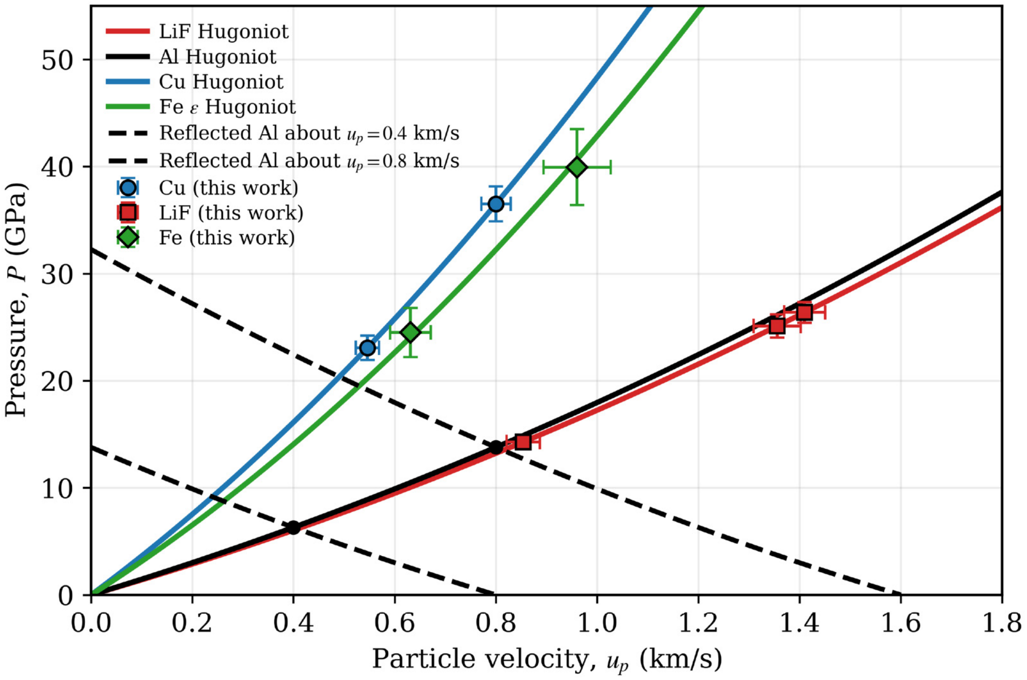

FIG. 16. Pressure–particle velocity (P–u_p) Hugoniot relations for Al, Cu, LiF, and ϵ-Fe. Dashed curves show reflected Al Hugoniots representing the approximate release from shocked aluminum states at $u_p = 400$ and $800\,\mathrm{m/s}$, corresponding to nominal Al flyer velocities of 800 and $1600\,\mathrm{m/s}$. Experimental peak-pressure states measured in this work for Cu, LiF, and Fe using amplifier configurations are shown. This construction allows comparison between pressures achieved with an amplifier driven by an $800\,\mathrm{m/s}$ Al flyer and those attainable through direct Al impact at the same velocity or at the approximate upper limit of the present gun system ($\sim 1600\,\mathrm{m/s}$).

VI. CONCLUSION

A pressure amplification method is presented, capable of extending the operational pressure ranges of single-stage gas gun/launchers to regimes previously only accessible with two-stage systems.

X-ray PCI was carried out at the ESRF to probe the internal shock dynamics of both the 45° and 75° cone angle amplifier variants, as well as the transmitted shock through PMMA targets. The shock front evolution captured through the PCI is in agreement with that predicted by the hydrodynamic simulations validating the predictive capabilities.

PDV measurements of shocked samples showed peak pressures of 37 and 40 GPa in Cu and Fe foils, respectively, as well as 27 GPa in LiF demonstrating 4.3 times pressure enhancement relative to direct impact opening new avenues for dynamic material studies and shock physics research using SSGG drivers.

ACKNOWLEDGMENTS

The authors acknowledge the European Synchrotron Radiation Facility (ESRF) for provision of beamtime under Proposal No. MI1464 and thank the beamline staff for their assistance and support during the Shock BAG experiment. The authors also gratefully acknowledge the Department of Engineering Science at the University of Oxford for access to and use of the single-stage gas launcher facility, supported by EPSRC and First Light Fusion under the AMPLIFI Prosperity Partnership—EP/X025373/1.

AUTHOR DECLARATIONS

Conflict of Interest

The authors have no conflicts to disclose.

Author Contributions

B. Dias: Conceptualization (equal); Data curation (equal); Formal analysis (lead); Investigation (equal); Methodology (equal); Validation (equal); Writing – original draft (lead); Writing – review & editing (lead). **R. L. Doherty:** Conceptualization (equal); Data curation (equal); Formal analysis (equal); Investigation (equal); Software (equal); Validation (equal); Writing – original draft (equal); Writing – review & editing (equal). **J. Shadbolt:** Data curation (equal); Investigation (equal); Validation (equal); Writing – review & editing (supporting). **V. Beltrán:** Conceptualization (equal); Investigation (equal); Methodology (equal); Software (equal). **E. Escauriza:** Conceptualization (equal); Data curation (equal); Formal analysis (equal); Investigation (equal); Methodology (equal); Validation (equal); Writing – review & editing (supporting). **D. J. Chapman:** Data curation (equal); Investigation (equal); Methodology (equal); Supervision (equal); Validation (equal); Writing – original draft (equal); Writing – review

& editing (equal). **D. E. Eakins:** Data curation (equal); Investigation (equal); Supervision (equal); Validation (equal); Writing – review & editing (supporting). **A. Rack:** Conceptualization (equal); Investigation (equal); Supervision (equal); Validation (equal). **H. W. Doyle:** Conceptualization (equal); Methodology (equal); Project administration (equal); Supervision (equal); Validation (equal); Writing – review & editing (supporting). **M. G. Gorman:** Formal analysis (equal); Investigation (equal); Methodology (equal); Supervision (equal); Writing – original draft (equal); Writing – review & editing (equal).

DATA AVAILABILITY

The x-ray PCI datasets acquired at the ESRF are available through the ESRF Data Portal under DOI: 10.15151/ESRF-ES-1729371531. Additional supporting materials are available from the corresponding author upon reasonable request.

APPENDIX A: VELOCITY DETERMINATION

Shock pressures were determined from velocity histories measured using photon Doppler velocimetry (PDV). Velocities were extracted from the free-surface or particle velocity traces by manual interpretation of the velocity–time profiles.

For Cu samples, the free-surface velocity v_{fs} was measured and converted to particle velocity using[40]

$$u_p = \frac{v_{fs}}{2}. \tag{A1}$$

For Fe samples, the measured quantity was also the free-surface velocity v_{fs}. The particle velocity was inferred using a material-specific free-surface relation[21]

$$u_p = \frac{v_{fs}}{1.97}. \tag{A2}$$

For LiF samples, particle velocity u_p was obtained directly from the velocity history without free-surface conversion.

Two independent uncertainty contributions were considered for all cases:

- A fixed instrumental PDV uncertainty of ±20 m/s.
- An uncertainty associated with manual interpretation of features in the velocity trace, quantified as the variation between the minimum and maximum velocities within the identified quasi-steady region.

These contributions were treated as independent and combined in quadrature:

$$\sigma_{u_p} = \sqrt{\sigma^2_{\mathrm{PDV}} + \sigma^2_{\mathrm{graph}}}. \tag{A3}$$

APPENDIX B: HUGONIOT RELATIONS

Shock pressures were determined using linear U_s–u_p Hugoniot relations of the form

$$U_s = c_0 + s u_p, \tag{B1}$$

where U_s is the shock velocity, u_p is the particle velocity, c_0 is the bulk sound speed, and s is the linear Hugoniot slope parameter.

Reference Hugoniot datasets were obtained from the Rusbank database. For Cu, LiF, and post-transition Fe, data were restricted to pressures below 100 GPa to ensure that fitted parameters were representative of the pressure regime relevant to the present experiments (typically ∼20–40 GPa). Linear regression was performed on the filtered dataset to determine c_0 and s, including the covariance between fitted parameters.

APPENDIX C: PRESSURE DETERMINATION: PRINCIPAL HUGONIOT

For Cu and LiF, shock pressure was calculated using the Rankine–Hugoniot momentum relation

$$P = \rho_0 u_p U_s, \tag{C1}$$

which, using Eq. (B1), becomes

$$P = \rho_0 u_p (c_0 + s u_p), \tag{C2}$$

where ρ_0 is the initial density of the material.

APPENDIX D: SPECIAL CASE: IRON (PHASE TRANSITION AND RESHOCK)

Iron undergoes the $\alpha \to \epsilon$ phase transition near 13 GPa. For iron, a two-step reshock model was employed based directly on the Rankine–Hugoniot conservation equations.

First, the pressure at the phase-transition state (P_1) was calculated using a pre-transition (α-Fe) Hugoniot fit:[21]

$$U_s = 4.460 + 1.720 u_p. \tag{D1}$$

The pressure at state 1 was, therefore,

$$P_1 = \rho_0 u_1 U_{s1}. \tag{D2}$$

The density at the phase-transition state (ρ_1) was calculated directly from Rankine–Hugoniot mass conservation,

$$\rho_1 = \frac{\rho_0 U_{s1}}{U_{s1} - u_1}, \tag{D3}$$

ensuring internal consistency between the pre-transition Hugoniot parameters and the reshock calculation.

For the second shock (reshock) to the final state (P_2), the momentum jump relation between states 1 and 2 was used:

$$P_2 = P_1 + \rho_1 (U_2 - u_1)(u_2 - u_1), \tag{D4}$$

where u_1 and u_2 are the particle velocities at states 1 and 2.

The shock velocity U_2 was estimated using the post-transition (ϵ-Fe) Hugoniot fit:

$$U_s = 3.816\,53 + 1.627\,37 u_p. \tag{D5}$$

This formulation treats the final state as a true reshock from the α–ϵ transition state, rather than assuming that the final state lies on a single principal Hugoniot from ambient conditions.

APPENDIX E: REFERENCE-STATE COMPARISON AND AMPLIFICATION RATIO (AR)

To compare peak pressures across different materials on a consistent basis, an equivalent pressure in each sample was estimated for a common reference state in the aluminum driver. The aluminum particle velocity was taken as $u_{p,0} = 0.4$ km/s, corresponding to a shocked aluminum pressure of approximately $P_{\mathrm{Al},0} \approx 6$ GPa from Eq. (C1) with the aluminum Hugoniot parameters in Table IV.

For each sample material $M \in \{\mathrm{Cu}, \mathrm{LiF}, \mathrm{Fe}\}$, an equivalent sample pressure $P_{\mathrm{eq}}(M)$ was obtained by intersecting the aluminum release with the principal Hugoniot of the sample:

$$P_{\mathrm{rel,Al}}(u^*) = P_{H,M}(u^*), \tag{E1}$$

where u^* is the interface particle velocity at which the two curves intersect. The corresponding equivalent sample pressure is then

$$P_{\mathrm{eq}}(M) = P_{H,M}(u^*). \tag{E2}$$

This procedure maps the reference aluminum state ($\sim$6 GPa) to the pressure that would be supported in each material at a release-matched interface, enabling direct comparison to the experimentally inferred peak sample pressures.

TABLE IV. Material parameters used for Hugoniot and reshock calculations. For Fe, ρ_1 is computed from Eq. (D2) using the α-Fe Hugoniot.

Material	ρ_0 (g/cm^3)	c_0 (km/s)	s	corr(c_0, s)
Al	2.71	5.293	1.358	−0.899
Cu	8.93	3.914	1.495	−0.901
LiF	2.65	5.159	1.347	−0.911
Fe (α)	7.87	4.460	1.720	…
Fe (ϵ)	…	3.817	1.627	−0.967

APPENDIX F: UNCERTAINTY PROPAGATION

Uncertainties in pressure were propagated using first-order (linear) error propagation. A summary of the dominant uncertainty contributions is provided in Table V.

For principal Hugoniot calculations (Cu, LiF), the total variance in pressure was calculated as

$$\sigma_P^2 = \left(\frac{\partial P}{\partial u_p}\sigma_{u_p}\right)^2 + \left(\frac{\partial P}{\partial c_0}\sigma_{c_0}\right)^2 + \left(\frac{\partial P}{\partial s}\sigma_s\right)^2 + 2\frac{\partial P}{\partial c_0}\frac{\partial P}{\partial s}\mathrm{Cov}(c_0, s). \tag{F1}$$

For iron reshock calculations, additional uncertainty contributions arise from

- uncertainty in u_1 and u_2,
- uncertainty in post-transition c_0 and s (including covariance),
- propagated uncertainty in U_2, and
- propagation through the mass-conservation calculation of ρ_1.

TABLE V. Summary of dominant uncertainty contributions in pressure determination and reference-state comparison.

Source	Typical magnitude	Notes
PDV velocity	±20 m/s	Instrumental limit
Graph interpretation	10–60 m/s	Shot dependent
c_0, s fit	1–3% in P	Includes covariance
Reshock terms (Fe)	2%–5%	u_1, u_2, and U_2 propagation
Al release proxy (P_{eq})	Few %	Al c_0, s uncertainty

For the reference-state comparison, uncertainty in $P_{\mathrm{eq}}(M)$ arises from uncertainty in the aluminum Hugoniot parameters (c_0, s and their covariance) propagated through the implicit intersection condition. The uncertainty in AR was then obtained by combining the fractional uncertainties in P_{peak} and $P_{\mathrm{eq}}(M)$ in quadrature.

REFERENCES

[1] L. Barilaro, M. Wylie, and T. Shafeeg, Appl. Sci. **13**, 7664 (2023).

[2] H. F. Swift, in *High-Pressure Shock Compression of Solids VIII: The Science and Technology of High-Velocity Impact* (Springer, 2005), pp. 1–35.

[3] D. Narayan and N. Bhatnagar, in *International Symposium on Plasticity and Impact Mechanics* (Springer, 2022), pp. 517–535.

[4] J. Carmona, M. Cook, J. Schmoke, K. Harper, J. Reay, L. Matthews, and T. Hyde, "Impact studies using a one stage light gas gun," arXiv:physics/0401161 (2004).

[5] S. C. Gupta, R. Agarwal, J. Gyanchandani, S. Roy, N. Suresh, S. Sikka, A. Kakodkar, and R. Chidambaram, in *Shock Compression of Condensed Matter–1991* (Elsevier, 1992), pp. 839–842.

[6] A. Lockrey, "Hypervelocity light gas gun—Modelling and design of a hypervelocity light gas gun test facility," Ph.D. thesis (University of Southampton, 2022).

[7] A. V. Pavlenko, S. I. Balabin, O. E. Kozelkov, and D. N. Kazakov, Instrum. Exp. Tech. **56**, 482 (2013).

[8] J. A. Rogers, N. T. Bass, M. L. Wiest, Z. Wantz, J. W. Wilkerson, and T. E. Lacy, Jr., Int. J. Impact Eng. **185**, 104861 (2024).

[9] B. Dias, T. Ringrose, O. Nash, J. Read, M. Gorman, C. Bradley, G. Burdiak, P. Jarvis, J. Shadbolt, J. Skidmore *et al.*, Next Res. **5**, 101351 (2026).

[10] A. J. Piekutowski and K. L. Poormon, Int. J. Impact Eng. **33**, 615 (2006).

[11] T. Moritoh, N. Kawai, K. G. Nakamura, and K.-I. Kondo, Rev. Sci. Instrum. **72**, 4270 (2001).

[12] D. W. Bogdanoff, "Design of a two-stage light gas gun for muzzle velocities of 10–11 km/s," Technical Note ARC-E-DAA-TN35142 (NASA Ames Research Center, Moffett Field, CA, 2016) presented at the Aeroballistic Range Association Meeting.

[13] A. Rack, B. Lukić, D. Chapman, J. Strucka, Y. Yao, K. Mughal, D. Maler, S. Efimov, O. Belozerov, Y. Krasik *et al.*, High Pressure Res. **44**, 400 (2024).

[14] N. V. Bykov, A. S. Karneychik, A. A. Makarov, and M. S. Tovarnov, J. Appl. Mech. Tech. Phys. **60**, 768 (2019).

[15] P. Giannuzzi, AIP Conf. Proc. **3066**, 480005 (2024).

[16] M. Brasseur, M. Vandenboomgaerde, C. Mariani, D. C. Barros, D. Souffland, and G. Jourdan, Exp. Fluids **62**, 156 (2021).

[17] F. Veloso, V. Rosales, M. Favre, and J. Valenzuela, Phys. Rev. E **110**, 065210 (2024).

[18] E. M. Escauriza, M. P. Olbinado, M. E. Rutherford, D. J. Chapman, J. C. Jonsson, A. Rack, and D. E. Eakins, Appl. Opt. **57**, 5004 (2018).

[19] B. Lukić, M. Blasone, Y. Duplan, P. Forquin, E. Escauriza, M. Rutherford, D. Chapman, D. Eakins, M. Olbinado, and A. Rack, in *EPJ Web of Conferences* (EDP Sciences, 2021), Vol. 250, p. 01014.

[20] D. Dolan, Rev. Sci. Instrum. **91**, 051501 (2020).

[21] S. A. Thomas, M. C. Hawkins, M. K. Matthes, G. T. Gray, and R. S. Hixson, J. Appl. Phys. **123**, 175902 (2018).

[22] M. G. Gorman, G. C. Burdiak, N. Niasse, V. Beltrán, R. L. Doherty, J. R. Allison, J. W. Skidmore *et al.*, J. Appl. Phys. **139**, 025902 (2026).

[23] H. Hornung, Annu. Rev. Fluid Mech. **18**, 33 (1986).

[24] M. S. Ivanov, D. Vandromme, V. M. Fomin, A. N. Kudryavtsev, A. Hadjadj, and D. V. Khotyanovsky, Shock Waves **11**, 199 (2001).

[25] R. E. Setchell, E. Storm, and B. Sturtevant, J. Fluid Mech. **56**, 505–522 (1972).

[26] D. Q. Duong and B. E. Milton, Exp. Fluids **3**, 161 (1985).

[27] H. Bellenbaum, M. Read, N. Niasse, S. Barrett, N. Hawker, N. Joiner, D. Chapman *et al.*, High Energy Density Phys. **53**, 101159 (2024).

[28] S. Faik, A. Tauschwitz, and I. Iosilevskiy, Comput. Phys. Commun. **227**, 117 (2018).

[29] D. A. Chapman, J. D. Pecover, N. Chaturvedi, N. Niasse, M. P. Read, D. H. Vassilev, J. P. Chittenden, N. Hawker, and N. Joiner, Phys. Plasmas **28**, 072702 (2021).

[30] M. J. Berger, J. H. Hubbell, S. M. Seltzer *et al.*, "XCOM: Photon cross sections database," (2010), NIST Standard Reference Database 8 (XGAM); see https://dx.doi.org/10.18434/T4D01F.

[31] P. Willmott, *An Introduction to Synchrotron Radiation: Techniques and Applications* (John Wiley & Sons, 2019).

[32] M. Wulff, F. Schotte, G. Naylor, D. Bourgeois, K. Moffat, and G. Mourou, Nucl. Instrum. Methods Phys. Res., Sect. A **398**, 69 (1997).

[33] M. E. Rutherford, D. J. Chapman, T. G. White, M. Drakopoulos, A. Rack, and D. E. Eakins, J. Synchrotron Radiat. **23**, 685 (2016).

[34] P. Cloetens, R. Barrett, J. Baruchel, J.-P. Guigay, and M. Schlenker, J. Phys. D: Appl. Phys. **29**, 133 (1996).

[35] L. Farbaniec, Y. Xu, J. Zhou, D. Macdougall, S. Patsias, N. Petrinic, C. Siviour, A. Pellegrino, and D. E. Eakins, Int. J. Impact Eng. **195**, 105139 (2025).

[36] F. Bagusat, M. Sauer, S. Bauer, and S. Hiermaier, in *Dynamic Behavior of Materials* (Elsevier, 2024), pp. 269–294.

[37] D. G. Hicks, T. R. Boehly, P. M. Celliers, D. K. Bradley, J. H. Eggert, R. S. McWilliams, R. Jeanloz, and G. W. Collins, Phys. Rev. B: Condens. Matter Mater. Phys. **78**, 174102 (2008).

[38] J. A. Hawreliak, J. M. Winey, Y. Toyoda, K. Zimmerman, and Y. M. Gupta, J. Appl. Phys. **136**, 165902 (2024).

[39] M. A. Meyers, *Dynamic Behavior of Materials* (John Wiley & Sons, 1994).

[40] S.-N. Luo, L.-B. Han, Y. Xie, Q. An, L. Zheng, and K. Xia, J. Appl. Phys. **103**, 093530 (2008).

[41] G. I. Kerley, "Calculation of release adiabats and shock impedance matching," arXiv:1306.6913 (2013).

[42] P. A. Rigg, M. D. Knudson, R. J. Scharff, and R. S. Hixson, J. Appl. Phys. **116**, 033515 (2014).

[43] D. Bancroft, E. L. Peterson, and S. Minshall, J. Appl. Phys. **27**, 291 (1956).

[44] X. Liu, T. Mashimo, N. Kawai, T. Sano, and X. Zhou, J. Appl. Phys. **124**, 215101 (2018).

[45] T. Takahashi and W. A. Bassett, Science **145**, 483 (1964).

[46] R. L. Clendenen and H. Drickamer, J. Phys. Chem. Solids **25**, 865 (1964).

[47] L. M. Barker and R. E. Hollenbach, J. Appl. Phys. **45**, 4872 (1974).

[48] R. F. Smith, J. H. Eggert, D. C. Swift, J. Wang, T. S. Duffy, D. G. Braun, R. E. Rudd, D. B. Reisman, J.-P. Davis, M. D. Knudson *et al.*, J. Appl. Phys. **114**, 223507 (2013).

[49] Y. B. Zel'Dovich and Y. P. Raizer, *Physics of Shock Waves and High-Temperature Hydrodynamic Phenomena* (Courier Corporation, 2002).

[50] S. P. Marsh, *LASL Shock Hugoniot Data* (University of California Press, 1980), Vol. 5.